ADVANCED FUNCTIONAL MATERIALS
www.afm-journal.de

A Single-Component Sb/Ho: $Cs_2Na_{0.9}Ag_{0.1}(In/Bi)Cl_6$ White Phosphor with a Record Color Rendering Index of 97.4

Manjia Zhang, Shilin Jin, Tao Pang, Bing Lin, Tianmin Wu, Lingwei Zeng, Lei Lei, and Daqin Chen**

The study on phosphors-converted white light-emitting diodes (pc-WLEDs) using lead-free double perovskites (DPs) as single-component white phosphors is widely concerned. However, the photoluminescence quantum yields (PLQY) of white luminescence and color rendering index (CRI) of WLED are not satisfactory. Herein, a new Sb/Ho: $Cs_2Na_{0.9}Ag_{0.1}(In/Bi)Cl_6$ single-component white phosphor with the highest PLQY of 93% and a record CRI of 97.4 is reported. Experimental data and theoretical calculations evidence that in addition to broadband yellow emission of the self-trapped exciton (STE) recombination, the material also exhibits blue emission from Sb^{3+}: $^3P_1 \rightarrow {}^1S_0$ transition and red one assigned to Ho^{3+}: $^5F_5 \rightarrow {}^5I_8$ transition. Steady-state and time-resolved PL spectra verify the existence of two energy transfer channels from both Sb^{3+} and STE to Ho^{3+} dopants. As a demo, Sb/Ho: $Cs_2Na_{0.9}Ag_{0.1}(In/Bi)$ Cl6-based WLED is constructed, showing excellent comprehensive optical performance with specially improved saturation red index R9 and blue one R12. This work provides a novel single-component rare-earth doped DP white phosphor for high CRI full-spectrum solid-state lighting.

1. Introduction

Lighting plays an irreplaceable role in human life and continues to develop with the advance of technologies.[1] Currently, pc-WLEDs have been commercialized for the advantages of low energy consumption, long working life, and environmental friendliness.[2] With the pursuit of high-quality white luminescence, full-spectrum sun-like lighting with high CRI has become highly desirable.[3] Up to now, the most common method for WLED is to couple polychromatic phosphors (blue, green, yellow, and red) with commercial GaN-based semiconductor LED chip (blue: 450 nm or ultraviolet: 365 nm) to compensate for the spectral profiles.[4–7] However, this strategy suffers from high cost and low efficiency owing to the energy reabsorption and adverse interactions among multiple optical materials.[8] Therefore, it is urgent to develop a highly efficient single-component white phosphor with high CRI full-spectrum emitting.[9]

Recently, lead-free DP has been recognized as a promising single-component white phosphor material due to its exceptional broadband STE recombination and non-toxicity.[10] Among various DPs, $Cs_2AgInCl_6$ can produce yellow luminescence with PLQY up to 86% by incorporating Na^+/Bi^{3+} dopants.[11] However, when it was used as a single-component white phosphor, there still exists an issue of insufficient blue and red-emitting components. Notably, Sb^{3+} with ns^2 electron configuration has garnered significant attention as a luminescent

M. Zhang, S. Jin, B. Lin, D. Chen
College of Physics and Energy
Fujian Normal University
Fuzhou, Fujian 350117, China
E-mail: dqchen@fjnu.edu.cn

T. Pang
Huzhou Key Laboratory of Materials for Energy Conversion and Storage
College of Science
Huzhou University
Huzhou, Zhejiang 313000, China

T. Wu
Key Laboratory of Opto-Electronic Science and Technology for Medicine of Ministry of Education
College of Photonic and Electronic Engineering
Fujian Normal University
Fuzhou, Fujian 350117, China
E-mail: wtm@fjnu.edu.cn

L. Zeng
School of Chemistry and Chemical Engineering
Hunan University of Science and Technology
Xiangtan 411201, China

L. Lei
Institute of Optoelectronic Materials and Devices
China Jiliang University
Hangzhou 310018, China

D. Chen
Fujian Provincial Collaborative Innovation Center for Advanced High-Field Superconducting Materials and Engineering
Fuzhou, Fujian 350117, China

D. Chen
Fujian Provincial Engineering Technology Research Center of Solar Energy Conversion and Energy Storage
Fuzhou, Fujian 350117, China

The ORCID identification number(s) for the author(s) of this article can be found under https://doi.org/10.1002/adfm.202407584

DOI: 10.1002/adfm.202407584

Table 1. Comparison of PLQY and CCT & CRI in WLEDs fabricated with DP materials. The excitation wavelength of the LED chip is also tabulated.

Materials	PLQY [%]	Chip wavelength	CCT [K]	CRI	Ref.
Bi/Ho: $Cs_2Ag_{0.6}Na_{0.4}InCl_6$	57	365 nm	/	75.4	2a
Er: $Cs_2Ag_{0.6}Na_{0.4}$InCl6	71	420 nm	5760	60	8
Sb/Tb/Ho: $Cs_2NaInCl_6$	/	320 nm	/	86.6	10
$Cs_2Ag_{0.6}Na_{0.4}0InCl_6$	86	410 nm	4054	/	11
Sb/Ho/Er: $Cs_2NaInCl_6$	70	310 nm	4608	/	16
Sb/Sm: $Cs_2NaInCl_6$	/	310 nm	8035	82	17
$Cs_2AgIn_{0.833}Bi_{0.167}Cl_6$	39	400 nm	3260	85	21
Bi: $Cs_2Ag_{0.7}Na_{0.3}InCl_6$	87	370 nm	4347	87.8	22
Sb/Mn/Tb: $Cs_2NaInCl_6$	/	310 nm	3371	89.2	23
Sb/Ho: Cs_2KInCl_6	90	315 nm	5210	90	24
Bi: $Cs_2AgScCl_6$	60	397 nm	4100	90	25
Sb/Mn/Er/Ho: $Cs_2NaInCl_6$	/	415 nm	/	/	26
Sb/Ho: $Cs_2Na_{0.9}Ag_{0.1}$(In/Bi)Cl_6	93	365 nm	3781	97.4	This work

center for blue emission.[12–14] For instance, doping Sb^{3+} into $Cs_2NaInCl_6$ leads to high-efficiency blue emission with PLQY of 75%.[15] Unfortunately, the exact mechanism for blue emission in DP materials after Sb^{3+} doping is still controversial. On the other hand, rare earth (RE) ions with $4f^n$ electron configurations show multiple excited states to produce abundant multicolor emissions to compensate for the lacking emitting components for full-spectrum lighting, but suffer from low absorption & emission ability owing to parity-forbidden 4f-4f transitions. A universal solution is to sensitize RE ions by semiconductors, such as DP materials.[16–20] However, as tabulated in **Table 1**, it is still highly desirable to develop single-component DP materials to achieve white-light luminescence with synergistic ultra-high CRI and PLQY.

Herein, a novel single-component Sb/Ho: $Cs_2Na_{0.9}Ag_{0.1}$(In/Bi)Cl_6 white phosphor with a high PLQY of 93% was developed for the first time. Upon UV light excitation, the product can simultaneously produce blue emission originated from Sb^{3+}: $^3P_1 \rightarrow {}^1S_0$ transition, broadband yellow emission assigned to STE recombination, and multiple emissions including a dominant red one owing to Ho^{3+}: $^5F_J \rightarrow {}^5I_8$ transitions (J = 3, 4, 5: 490, 545, and 658 nm, respectively), leading to full-spectrum white-light luminescence with a record CRI of 97.4 among previously reported DP materials[2,8,10,11,16,17,21–26] (Table 1). Both density functional theory (DFT) calculations and spectroscopic data evidence that local structure engineering of DP via Sb^{3+}/Bi^{3+} co-doping results in blue/yellow emissions and dual-channel energy transfer from both Sb^{3+} and STE leads to Ho^{3+} emissions to compensate for the white-light spectrum. Finally, the Sb/Ho: $Cs_2Na_{0.9}Ag_{0.1}$(In/Bi) Cl6-based WLED is constructed to demonstrate its potential application in high CRI full-spectrum lighting.

2. Results and Discussion

Sb/Ho: $Cs_2Na_{0.9}Ag_{0.1}$(In/Bi)Cl_6 was synthesized by a modified coprecipitation method. In a typical synthesis, stoichiometric amounts of $InCl_3$, AgCl, $BiCl_3$, NaCl, $SbCl_3$, and $HoCl_3$ are dissolved in hydrochloric acid at 100 °C. After adding CsCl solution, the precipitation was formed after the reaction for 20 min. It is worth noting that the synthesis of DPs requires a light-blocking glass bottle to prevent the oxidation of silver chloride. Schematic crystal structure of $Cs_2Na_{0.9}Ag_{0.1}$(In/Bi)Cl_6 DP is shown in **Figure 1a**, where $[(Na/Ag)Cl_6]^{5-}$ and $[(In/Bi)Cl_6]^{3-}$ octahedrons alternately locate in the unit cell and Cs^+ ions occupy the center of the octahedral cavities. Sb^{3+} and Ho^{3+} ions are expected to substitute the lattice sites of In^{3+} based on the ionic equivalent charge and ionic radii. X-ray diffraction (XRD) patterns show that all the doped samples retain the face-centered cubic $Cs_2Na_{0.9}Ag_{0.1}InCl_6$ structure (Figure 1b; Figure S1, Supporting Information). Owing to different ionic radii such as In^{3+} (R = 0.80 Å), Bi^{3+} (R = 1.03 Å), Sb^{3+} (R = 0.76 Å), and Ho^{3+} (R = 0.90 Å), a slight shift of diffraction peak is detected after ion substitution of In^{3+} by Bi^{3+}, Sb^{3+}, and Ho^{3+} (Figure S1, Supporting Information). Scanning electron microscopy (SEM) image shows that the products are micron-size particles with polygonal morphology, and energy-dispersive X-ray (EDX) mappings confirm the uniform distribution of all elements Cs, Ag, Na, In, Cl, Bi, Sb, and Ho (Figure 1c). High-resolution transmission electron microscopy (HRTEM) image demonstrates high crystallinity of DP particles with a planar spacing of 0.210 nm corresponding to the (224) plane (Figure S2, Supporting Information). Typical Cs 3d, Na 1s, Ag 3d, In 3d, Bi 4f, and Cl 2p signal peaks are detected by high-resolution X-ray photoelectron spectroscopy (XPS), and additional Sb 3d and Ho 4d peaks are observed for the Sb/Ho: $Cs_2Na_{0.9}Ag_{0.1}$(In/Bi)Cl_6 DP (Figure S3, Supporting Information). All these results verify that Sb^{3+} and Ho^{3+} ions have successfully entered into the $Cs_2Na_{0.9}Ag_{0.1}$(In/Bi)Cl_6 crystal lattice. The nominal Ho/In doping ratio was set from 10.2% to 61.2%, which corresponds to the actual mole concentration from 0.33% to 2.24% measured by inductively coupled plasma mass spectrometry (ICP-MS, Table S1, Supporting Information). Only a small amount of Ho^{3+} ions are incorporated into the DP crystalline lattice, which may be due to highly different electronic configurations of Ho^{3+} dopants and In^{3+} ions.

The influence of Sb^{3+}/Ho^{3+} dopants on the optical properties of DP was investigated (Figure 1d). PL spectrum of $Cs_2Na_{0.9}Ag_{0.1}InCl_6$ shows both weak blue and yellow emission

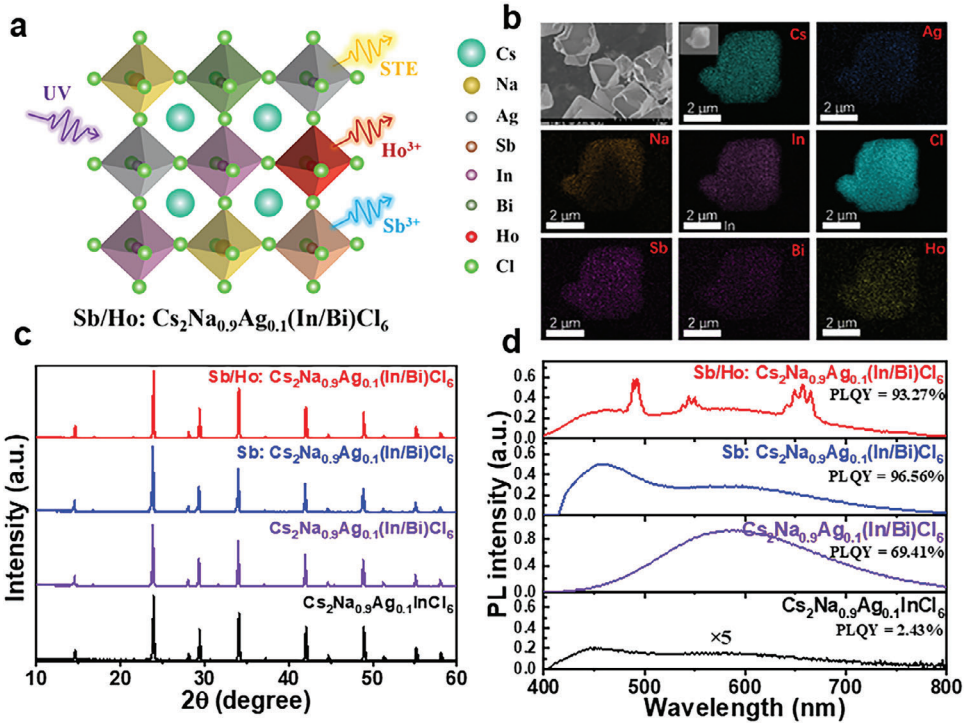

Figure 1. a) Schematic illustration of Sb/Ho: $Cs_2Na_{0.9}Ag_{0.1}(In/Bi)Cl_6$ DP crystal structure. b) XRD patterns of the undoped, Bi-doped, Sb/Bi co-doped, and Sb/Bi/Ho tri-doped $Cs_2Na_{0.9}Ag_{0.1}InCl_6$ DPs. c) SEM image and EDX mapping of Sb/Ho: $Cs_2Na_{0.9}Ag_{0.1}(In/Bi)Cl_6$. d) PL spectra of the undoped, Bi-doped, Sb/Bi co-doped, and Sb/Bi/Ho tri-doped $Cs_2Na_{0.9}Ag_{0.1}InCl_6$ DPs.

bands and the PLQY value is <3% (Figure S4a, Supporting Information). Upon a trace of (1 mol%) Bi^{3+} doping, yellow luminescence is dominant and the PLQY value reaches as high as 69.41% (Figure S4b, Supporting Information). Further incorporation of Sb^{3+} significantly enhances the blue emission, leading to efficient dual-emissions of blue and yellow with PLQY of 96.56% (Figure S4c, Supporting Information). Finally, Ho^{3+} co-doping produces extra three sharp emissions assigned to Ho^{3+}: $^5F_J \rightarrow {}^5I_8$ transitions (J = 3, 4, 5: 490, 545, and 658 nm, respectively) besides blue and yellow light emissions. The PLQY of Sb/Ho: $Cs_2Na_{0.9}Ag_{0.1}(In/Bi)Cl_6$ DP reaches as high as 93.27% (Figure S4d–f and Movie S1, Supporting Information), which is the highest value reported so far for the single-component white DP phosphors (Table 1). In addition, the absorption efficiency for the excitation light is calculated and provided in Table S2 (Supporting Information), which shows a 78% value for the Sb/Ho: $Cs_2Na_{0.9}Ag_{0.1}(In/Bi)Cl_6$ sample.

In order to better understand the intrinsic photophysical processes, a series of different Sb^{3+} and Ho^{3+} doped samples were prepared. **Figure** 2a shows the PL and PL excitation (PLE) spectra of Sb: $Cs_2Na_{0.9}Ag_{0.1}InCl_6$. There is a weak blue emission at 450 nm in the undoped sample, which is significantly enhanced after the Sb^{3+} dopants are added. Interestingly, the excitation band in the PLE spectrum is consistent with the Sb^{3+} absorption transition, where the excitation band at 280 nm corresponds to the vibration-allowed $^1S_0 \rightarrow {}^3P_2$ transition of Sb^{3+}, and that in the 300–360 nm range corresponds to the spin-orbit allowed $^1S_0 \rightarrow {}^3P_1$ transition. Due to the dynamic Jahn-Teller effect, the $^1S_0 \rightarrow {}^3P_1$ transition splits into typical two bands at 320 and 340 nm.[27,28] As a complement, UV–vis absorption spectra of Sb: $Cs_2Na_{0.9}Ag_{0.1}InCl_6$ samples have been recorded (Figure S5, Supporting Information). Three typical absorption bands assigned to $^1S_0 \rightarrow {}^1P_1$, $^1S_0 \rightarrow {}^3P_2$, and $^1S_0 \rightarrow {}^3P_1$ transitions of Sb^{3+} are observed, which is in good agreement with PLE spectra. These results indicate that the absorption and blue light emission occur within Sb^{3+} ions for the Sb: $Cs_2Na_{0.9}Ag_{0.1}InCl_6$ samples. In fact, we detected a trace of Sb^{3+} impurity in the $InCl_3$ reagent (Table S3, Supporting Information), confirming that the weak blue emission of the Sb-undoped $Cs_2Na_{0.9}Ag_{0.1}InCl_6$ sample indeed originates from impurity Sb^{3+}: $^3P_1 \rightarrow {}^1S_0$ transition. Notably, with an increase of Sb^{3+} content, PLQY of Sb: $Cs_2Na_{0.9}Ag_{0.1}InCl_6$ can reach as high as 71.16% (Table S4, Supporting Information). Impressively, with the introduction of 1 mol% Bi^{3+} ions, extra broadband yellow emission is detected besides blue one, which is attributed to STE recombination (Figure 2b, right). As a comparison, we prepared Bi^{3+} doped samples (Bi^{3+}: $Cs_2NaInCl_6$), which show only weak blue emission (Figure S6, Supporting Information). Therefore, the present yellow emission is believed to be attributed to STE emission rather than Bi^{3+} dopants. Notably, with an increase of Sb^{3+} concentration, the blue emission first gradually increases and then tends to weaken owing to the concentration quenching effect, while the STE yellow emission monotonously decreases for the Sb: $Cs_2Na_{0.9}Ag_{0.1}(In/Bi)Cl_6$ samples. PLE spectra by monitoring the yellow STE emission show a strong excitation band at 340 nm (Figure 2b, left), which originates from Bi^{3+}-promoted parity-allowed transition from valence band maximum (VBM) to conduction band minimum (CBM).[29] Interestingly, under UV light excitation, the Sb:

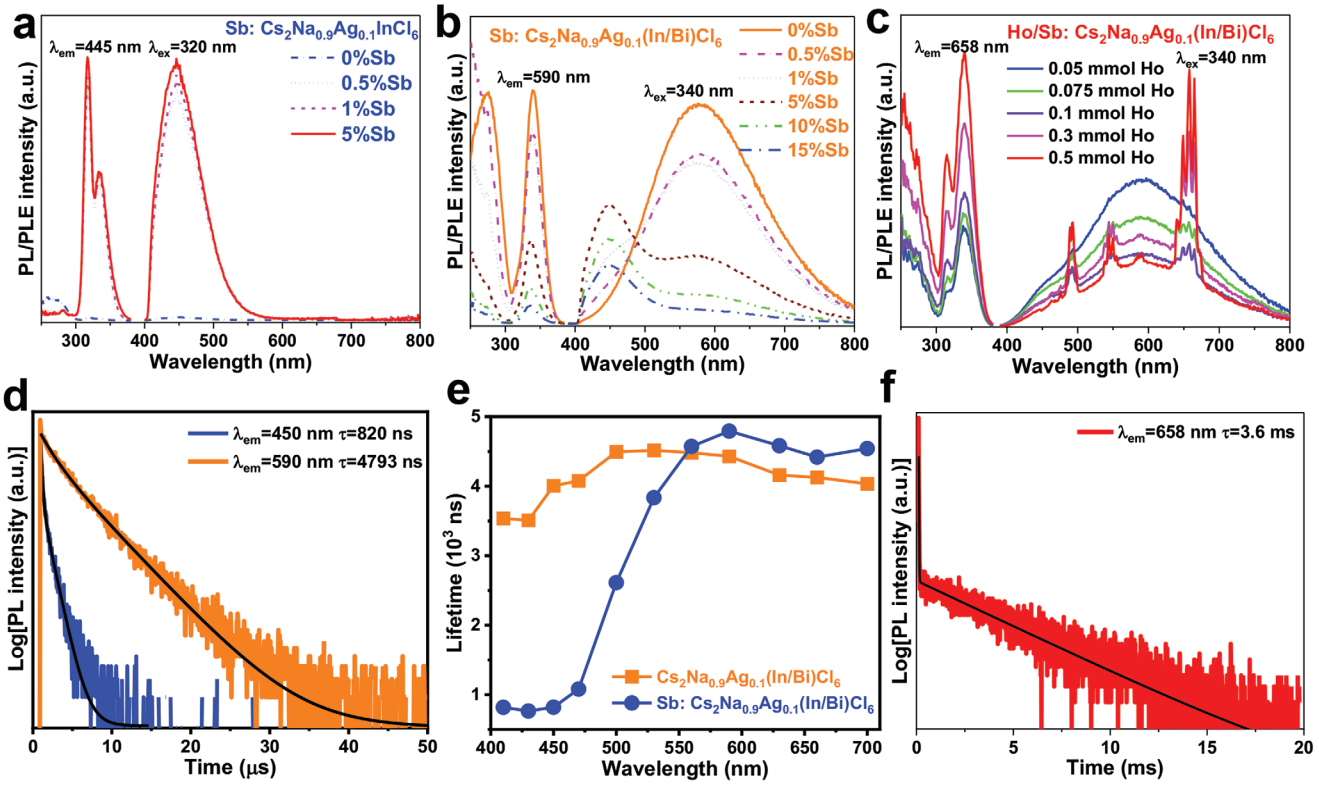

Figure 2. Sb^{3+}-doping content dependent PL/PLE spectra of a) Sb: $Cs_2Na_{0.9}Ag_{0.1}InCl_6$. and b) Sb: $Cs_2Na_{0.9}Ag_{0.1}(In/Bi)Cl_6$ samples. c) PL/PLE spectra of Sb/Ho: $Cs_2Na_{0.9}Ag_{0.1}(In/Bi)Cl_6$ with various Ho^{3+} doping contents. d) PL decay curves by monitoring Sb^{3+} (450 nm) and STE (590 nm) emissions for Sb: $Cs_2Na_{0.9}Ag_{0.1}(In/Bi)Cl_6$ sample. e) PL wavelength-dependent lifetimes for the Sb: $Cs_2Na_{0.9}Ag_{0.1}(In/Bi)Cl_6$ and $Cs_2Na_{0.9}Ag_{0.1}(In/Bi)Cl_6$ samples. f) PL decay curve by monitoring Ho^{3+} (658 nm) emission for the Sb/Ho: $Cs_2Na_{0.9}Ag_{0.1}(In/Bi)Cl_6$ sample.

$Cs_2Na_{0.9}Ag_{0.1}(In/Bi)Cl_6$ samples can yield different emitting colors changes from yellow to blue (including cold white for 1 mol% Sb^{3+} sample) with increase of Sb^{3+} concentration (Figure S7, Supporting Information). To compensate for the shortage of red-light components, Ho^{3+} dopants were incorporated into the Sb (1 mol%): $Cs_2Na_{0.9}Ag_{0.1}(In/Bi)Cl_6$ host. Importantly, with an increase in Ho^{3+} concentration, Ho^{3+} emissions monotonously enhance (Figure 2c, right). Compared to the sample without Ho^{3+} doping, the luminescence in the red spectral region assigned to Ho^{3+}: $^5F_5 \rightarrow {}^5I_8$ transition is significantly boosted for the Sb/Ho: $Cs_2Na_{0.9}Ag_{0.1}(In/Bi)Cl_6$ DPs. Notably, PLE spectra by monitoring 658 nm red emission show both characteristic excitation bands of Sb^{3+} ions and STE (Figure 2c, left), indicating the existence of energy transfer channels from both Sb^{3+} dopants and STEs to Ho^{3+} activators.

To explore the origin of these emission peaks, we monitored the PL decay curves of blue and yellow emissions for the Sb: $Cs_2Na_{0.9}Ag_{0.1}(In/Bi)Cl_6$ sample. As shown in Figure 2d, the PL lifetime of blue emission (820 ns) is on a nanosecond scale owing to parity-allow $sp \rightarrow s^2$ transition of Sb^{3+}[30,31] while that of yellow emission (4.8 μs) is on a microsecond scale ascribing to Jahn-Teller distortion-induced STE recombination.[2,29] We further recorded PL decay behaviors of different emitting wavelengths for the $Cs_2Na_{0.9}Ag_{0.1}(In/Bi)Cl_6$ and Sb: $Cs_2Na_{0.9}Ag_{0.1}(In/Bi)Cl_6$ samples (Figure 2e). The decay lifetimes for the emissions covering the blue and yellow spectral region remain ≈4 μs for the sample without Sb^{3+} doping. However, after Sb^{3+} doping, PL lifetimes in the blue spectral range are significantly shortened to below 1 μs, confirming that the origin of blue emission is due to Sb^{3+}: $^3P_1 \rightarrow {}^1S_0$ transition. To further prove that the blue emission comes from Sb^{3+}, we compared the decay behaviors of Sb: $Cs_2Na_{0.9}Ag_{0.1}InCl_6$ at low temperature (80 K) and room temperature (Figure S8, Supporting Information). It is worth noting that the luminescence decay at 80 K is far longer than that at room temperature. This is due to the involvement of Sb^{3+}: $^3P_0 \rightarrow {}^1S_0$ forbidden transition with long decay lifetime at low temperature,[32] certainly providing direct evidence of Sb^{3+} blue emission in the present case. Finally, a typical decay curve by monitoring Ho^{3+} 658 nm emission for the Sb/Ho: $Cs_2Na_{0.9}Ag_{0.1}(In/Bi)Cl_6$ sample was recorded (Figure 2f), which shows a long decay lifetime of 3.6 ms owing to its parity-forbidden 4f→4f transition.

To confirm the occurrence of energy transfer processes, 2D excitation-emission mapping for the undoped, Sb^{3+}-doped, Ho^{3+}-doped, Sb^{3+}/Ho^{3+} co-doped $Cs_2Na_{0.9}Ag_{0.1}(In/Bi)Cl_6$ samples were recorded, as shown in **Figures** 3a–c and S9 (Supporting Information). Evidently, STE and Sb^{3+} dopants yield broadband yellow and blue luminescence upon their respective excitation spectral ranges (Figure 3a,b), and Ho^{3+} activators emit multiple $^5F_J \rightarrow {}^5I_8$ narrowband emissions (Figure 3c), which are superposed upon the broadband spectrum. It can be clearly observed that the excitation of Ho^{3+} can cover both Sb^{3+} and STE excitation regions (Figure 3c). This can be seen intuitively by

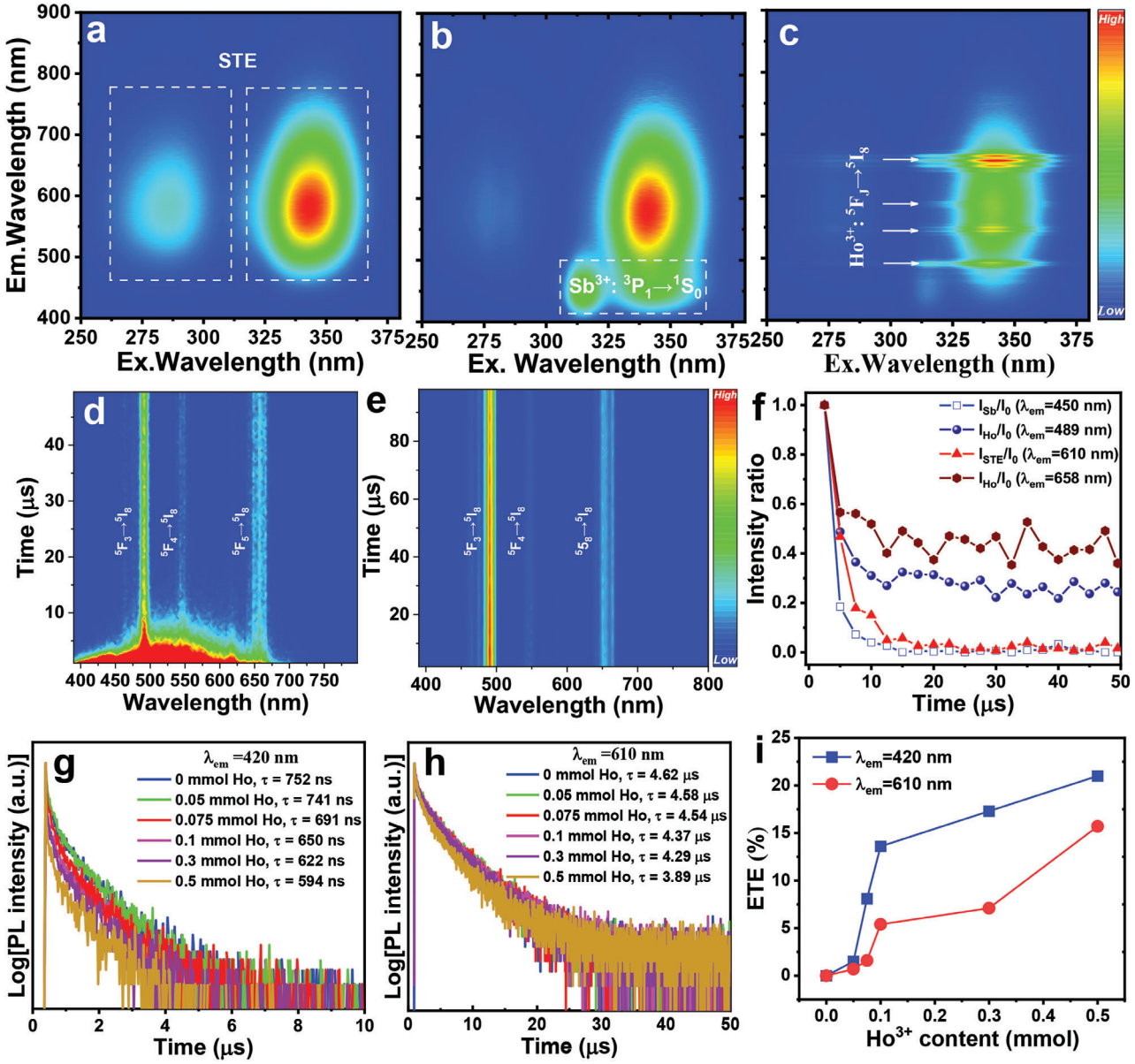

Figure 3. 2D excitation-emission mapping of a) $Cs_2Na_{0.9}Ag_{0.1}(In/Bi)Cl_6$, b) Sb: $Cs_2Na_{0.9}Ag_{0.1}(In/Bi)Cl_6$ and c) Sb/Ho: $Cs_2Na_{0.9}Ag_{0.1}(In/Bi)Cl_6$. TRPL mapping of Sb/Ho: $Cs_2Na_{0.9}Ag_{0.1}(In/Bi)Cl_6$ within time windows of d) 50 μs and e) 100μs. f) Variation of intensity ratios of Sb^{3+} (450 nm), STE (610 nm), or Ho^{3+} (658 nm) emission intensity relative to the initial one (I_0) over time. PL decay curves of Sb/Ho: $Cs_2Na_{0.9}Ag_{0.1}(In/Bi)Cl_6$ with various Ho^{3+} contents by monitoring g) 420 nm emission and h) 610 nm one. i) ET efficiency from Sb^{3+} or STE to Ho^{3+} dopants versus Ho^{3+} concentration.

monitoring the PLE spectra of the Sb/Ho co-doped sample at different emitting positions (450, 610, and 658 nm), as shown in Figure S10a (Supporting Information), providing direct evidence of simultaneous energy transfer from both Sb^{3+} dopants and STEs to Ho^{3+} activators. Time-resolved PL (TRPL) mapping of Sb/Ho: $Cs_2Na_{0.9}Ag_{0.1}(In/Bi)Cl_6$ was further measured in the spectral range from 390 to 800 nm. When the time window is set to 50 us, the decay profiles, including Sb^{3+}&STE broad bands and Ho^{3+} narrow bands centered at 490, 545, and 658 nm, are clearly observed (Figure 3d). When the time window is extended to 100 μs, only Ho^{3+} emissions are obviously observed (Figure 3e), which are present until the time window reaches 15 ms (Figure S10b, Supporting Information). PL intensity ratios of Sb^{3+}, STE, and Ho^{3+} emitting centers relative to the initial one within 50 μs decay time scale are compared. The results show that PL decay rates of the Sb^{3+} and STE are much faster than that of Ho^{3+}, and overall PL intensity is entirely contributed by Ho^{3+} PL after 15 μs decay (Figure 3f; Figure S10c, Supporting Information). To quantitatively determine energy transfer efficiency, PL decay curves by monitoring Sb^{3+}: $^3P_1 \rightarrow {}^1S_0$ transition (420 nm), STE recombination (610 nm) and Ho^{3+}: $^5F_5 \rightarrow {}^5I_8$ transition (658 nm) for the Sb/Ho: $Cs_2Na_{0.9}Ag_{0.1}(In/Bi)Cl_6$ samples doped with different Ho^{3+} contents were recorded, as shown in Figure 3g,h and Figure S10d (Supporting Information),

respectively. Evidently, the decays of both Sb^{3+} and STE become faster with an increase of Ho^{3+} concentration owing to the occurrence of extra energy transfer channels to Ho^{3+}, and the corresponding lifetimes decrease from 752 to 594 ns for Sb^{3+} and from 4.6 to 3.9 µs for STE (Table S5, Supporting Information). At the same time, the decay lifetime of Ho^{3+} shows a slight decrease owing to the concentration quenching effect (Figure S10d, Supporting Information). Herein, the reduction in decay lifetimes of Sb^{3+}: $^3P_1 \rightarrow {}^1S_0$ transition and STE recombination evidences that increasing Ho^{3+} doping concentration leads to enhanced energy transfer from Sb^{3+} and STE to Ho^{3+} activators. Correspondingly, energy transfer efficiency (ETE: η_t) can be evaluated by using the following equation[33]

$$\eta_t = 1 - \tau_1/\tau_0 \quad (1)$$

where τ_1 and τ_0 are the lifetimes of Sb^{3+}: $^3P_1 \rightarrow {}^1S_0$ transition or STE recombination in the presence and absence of Ho^{3+} dopants, respectively. With the increase of Ho^{3+} concentration, ETEs for both Sb^{3+}-to-Ho^{3+} and STE-to-Ho^{3+} increase gradually (Figure 3i, Table S6, Supporting Information), reaching 21% and 16%, respectively. As a consequence, the combination of residual blue emission of Sb^{3+} and yellow emission of STE together with ET-induced red emission of Ho^{3+} leads to pure white light (Figure S11, Supporting Information).

Furthermore, structural variations of $Cs_2NaInCl_6$ after Sb^{3+} and $Sb^{3+}/Ag^+/Bi^{3+}$ doping were studied via density-functional theory (DFT) calculations. The calculated projected density of states (DOS) and electronic band structures of $Cs_2NaInCl_6$, $Cs_2NaIn_{0.97}Sb_{0.03}Cl_6$, and $Cs_2Na_{0.91}Ag_{0.09}In_{0.94}Sb_{0.03}Bi_{0.03}Cl_6$ DPs are shown in Figure S12 (Supporting Information) and **Figure 4a,b**. In $Cs_2NaInCl_6$ DPs, the VBM and CBM comprised Cl-*3p* orbital and the hybrid states of Cl-*3p*, Na-*3s*, and In-*5s* orbitals (Figure S12a–c, Supporting Information), respectively. After Sb^{3+} doping ($Cs_2NaIn_{0.97}Sb_{0.03}Cl_6$), the CBM is very similar to $Cs_2NaInCl_6$ (Figure S12a–c, Supporting Information), while the VBM is mainly composed of the hybridization of Cl-*3p* and Sb-*5s* orbitals. Sb^{3+} doping narrows the electronic bandgap from 2.89 to 2.54 eV. Moreover, the calculated DOS and electronic band structure of $Cs_2NaIn_{0.97}Sb_{0.03}Cl_6$, as illustrated in Figure S12a,d,e (Supporting Information) clearly show that the VBM of $[SbCl_6]^{3-}$ appears above the host valence band, while the CBM of $[SbCl_6]^{3-}$ (Sb-*5p*) appears in a gap deep of the host conduction band. Current theoretical investigations show that the CBM-VBM gap of $[SbCl_6]^{3-}$ is 3.83 eV (Figure S12a,d,e, Supporting Information), which is between the split PLE (3.70–3.90 eV) and thus should be the origin of blue emission. For $Sb^{3+}/Ag^+/Bi^{3+}$ doped in $Cs_2NaInCl_6$ ($Cs_2Na_{0.91}Ag_{0.09}In_{0.94}Sb_{0.03}Bi_{0.03}Cl_6$) DP, the VBM is still derived from the Cl-*3p* and Sb-*5s* orbitals, while the CBM mainly stem from the hybridization of the Cl-*3p*, Na-*3s*, Ag-*5s* and In-*5s* states. A hybrid states composed of Cl-*3p*, Sb-*5p* and Bi-*6p* ($[BiCl_6]^{3-}$ and $[SbCl_6]^{3-}$ octahedra) appears, and CBM of $[BiCl_6]^{3-}$ is slightly above the CBM of $[SbCl_6]^{3-}$ (Figure 4a,b, Figure S12a, Supporting Information).

On the other hand, the substitution of metallic cations in the host usually induces Jahn-Teller-like octahedral distortions in metal-halide perovskites, thus leading to the formation of emissive self-trapped excitons, which are mainly responsible for the observed broadband luminescence. In $Cs_2NaInCl_6$, theoretical calculations show that both the excited electrons and holes are dispersed over the full real space, as illustrated in Figure 4c. For $Cs_2NaIn_{0.97}Sb_{0.03}Cl_6$, due to the similar ionic radii between Sb^{3+} with In^{3+}, the substitution of Sb^{3+} with In^{3+} does not induce large lattice distortion in $Cs_2NaInCl_6$. The electrons are therefore observed to remain strongly confined in $[InCl_6]^{3-}$ octahedrons over the full real space, whereas the holes are localized around $[SbCl_6]^{3-}$ octahedrons (Figure 4c). As a consequence, only Sb^{3+} blue emission rather than STE one is observed for the Sb: $Cs_2NaInCl_6$ DP. In comparison, significant lattice distortion occurs when Sb^{3+} and Bi^{3+} dopants replace In^{3+} ions in $Cs_2NaInCl_6$ DP ($Cs_2Na_{0.91}Ag_{0.09}In_{0.94}Sb_{0.03}Bi_{0.03}Cl_6$), since the ionic radius of Bi^{3+} [1.03 Å] is much larger than those of In^{3+} [0.80 Å] and Sb^{3+} [0.76 Å].[34,35] The occurrence of large octahedral deformation in $Cs_2Na_{0.91}Ag_{0.09}In_{0.94}Sb_{0.03}Bi_{0.03}Cl_6$ DP, therefore, provides a favorable environment for the production of STE state. Indeed, theoretical calculations clearly show that the Bi^{3+} doping is beneficial to significantly confining the spatial distribution of the STE state, in which the holes remain the localization around $[SbCl_6]^{3-}$ octahedrons while the electrons are distributed around $[InCl_6]^{3-}$ and $[AgCl_6]^{5-}$ octahedrons, as depicted in Figure 4c.

Based on the above-mentioned spectroscopic data and theoretical calculations, we proposed a white-light-emitting mechanism and energy transfer processes in the Sb/Ho: $Cs_2Na_{0.9}Ag_{0.1}(In/Bi)Cl_6$ DP, as illustrated in Figure 4d. The luminescence of $Cs_2NaInCl_6$ is weak owing to the forbidden transition from VBM to CBM. Upon Sb^{3+} doping, strong blue emission occurs, which originates from $^3P_1 \rightarrow {}^1S_0$ transition of Sb^{3+}; Further introducing Ag^+/Bi^{3+} ions leads to large deformation of $[SbCl_6]^{3-}$ & $[InCl_6]^{3-}$ & $[AgCl_6]^{5-}$ octahedrons and is attributed to the formation of STE state, resulting in bright yellow emission arising from STE recombination; Finally, the addition of Ho^{3+} dopants will produce extra strong red emission of Ho^{3+}: $^5F_5 \rightarrow {}^5I_8$ transition besides weak blue ($^5F_3 \rightarrow {}^5I_8$) and green ($^5F_4 \rightarrow {}^5I_8$) ones. Herein, two channels to transfer energy to Ho^{3+} dopants in the DP samples are proposed: one is an energy transfer from free exciton (FE) to STE and then to Ho^{3+}, and the other is a partial energy transfer from Sb^{3+} to Ho^{3+} (Figure 4d). As a consequence, the combination of tri-emitting states from Sb^{3+}, STE, and Ho^{3+} results in tunable white luminescence in the single-component Sb/Ho: $Cs_2Na_{0.9}Ag_{0.1}(In/Bi)Cl_6$ DP (Figure S11, Supporting Information).

In further work, the stability of Sb/Ho: $Cs_2Na_{0.9}Ag_{0.1}(In/Bi)Cl_6$ is evaluated. As shown in Figure S13 (Supporting Information), after the sample is exposed to air for 180 days, it's structure and spectral profile & intensity remain unchanged, confirming that the present DP material exhibits excellent environmental stability. Temperature-dependent (80–320 K) PL spectra of Sb/Ho:$Cs_2Na_{0.9}Ag_{0.1}(In/Bi)Cl_6$ DP are further recorded. As expected, PL intensities of all the tri-emitting states (Sb^{3+}, STE, and Ho^{3+}) show a tendency to decrease with elevation of temperature (Figure S14a, Supporting Information). Based on temperature-sensitive integrated PL intensity (Figure S14b, Supporting Information), the apparent exciton binding energy can be determined by fitting the data via the Arrhenius equation[36]

$$I(T) = \frac{I_0}{1 + A\exp\left(\frac{-E_b}{k_B T}\right)} \quad (2)$$

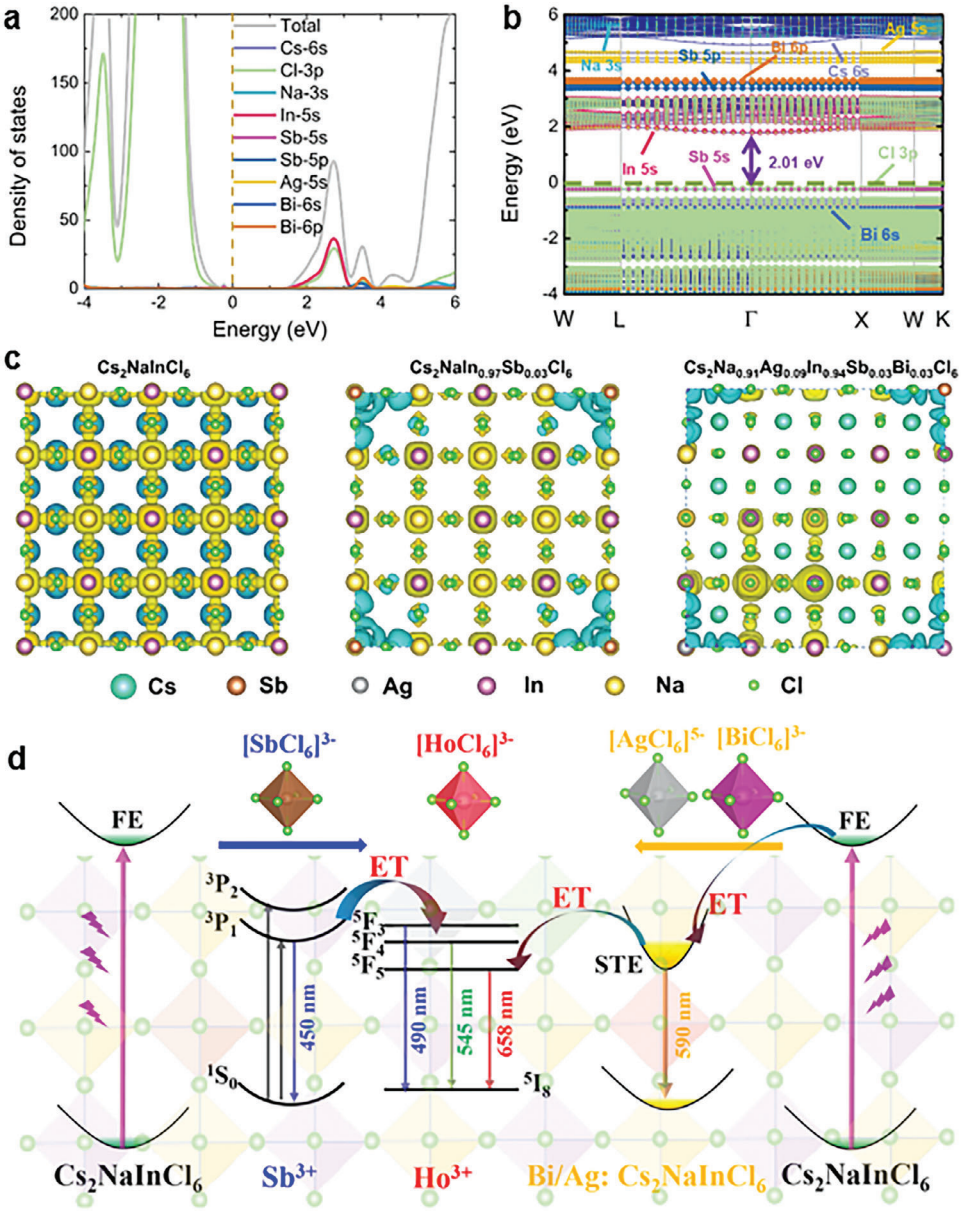

Figure 4. DFT-calculated a) projected DOS and b) electronic band structure for the $Cs_2Na_{0.91}Ag_{0.09}In_{0.94}Sb_{0.03}Bi_{0.03}Cl_6$ DP. c) STE in $Cs_2NaInCl_6$, $Cs_2NaIn_{0.97}Sb_{0.03}Cl_6$ and $Cs_2Na_{0.91}Ag_{0.09}In_{0.94}Sb_{0.03}Bi_{0.03}Cl_6$ DPs. d) The proposed photophysical processes of Sb/Ho: $Cs_2Na_{0.9}Ag_{0.1}$ (In/Bi)Cl_6 single-component white phosphor.

where I_0, k_B, and E_b represent the integrated PL intensity at 0 K, Boltzmann constant, and exciton binding energy, respectively, and A is a constant. Correspondingly, the apparent binding energy is extracted to be 221 meV (Figure S14b, Supporting Information), which is far larger than room temperature energy (26 meV) and indicates stable white-light luminescence with highly localized behaviors for the present Sb/Ho: $Cs_2Na_{0.9}Ag_{0.1}$(In/Bi)Cl_6 DP.

Benefiting from its integrated superior properties, we demonstrate the potential application of this material as a single-component white light emitter in lighting. Herein, the pc-WLED devices are fabricated by combining a 365 nm violet chip with un-doped, Sb^{3+} doped and Sb^{3+}/Ho^{3+} co-doped $Cs_2Na_{0.9}Ag_{0.1}$(In/Bi)Cl_6 DPs, which are designated as WLED1, WLED2 and WLED3, respectively. The electroluminescence (EL) spectra and photographs of the fabricated WLEDs at the driven current/voltage of 3 V/50 mA are presented in **Figure** 5a–c. As expected, blue emission of Sb^{3+}, broadband yellow emission of STE, and dominant red emission of Ho^{3+} are simultaneously detected for WLED3, which leads to bright full-spectrum white light emitting with chromaticity coordinates of (0.39, 0.38) located in the white region. As a comparison, the shortage of Sb^{3+} blue emission in WLED1 and Ho^{3+} deep-red emission in WLED2 results in the deviation of white light, as shown in CIE color coordinates (Figure S15, Supporting Information). Accordingly, the CRI value of R_a increases from 82.7 (WLED1) to 89.4

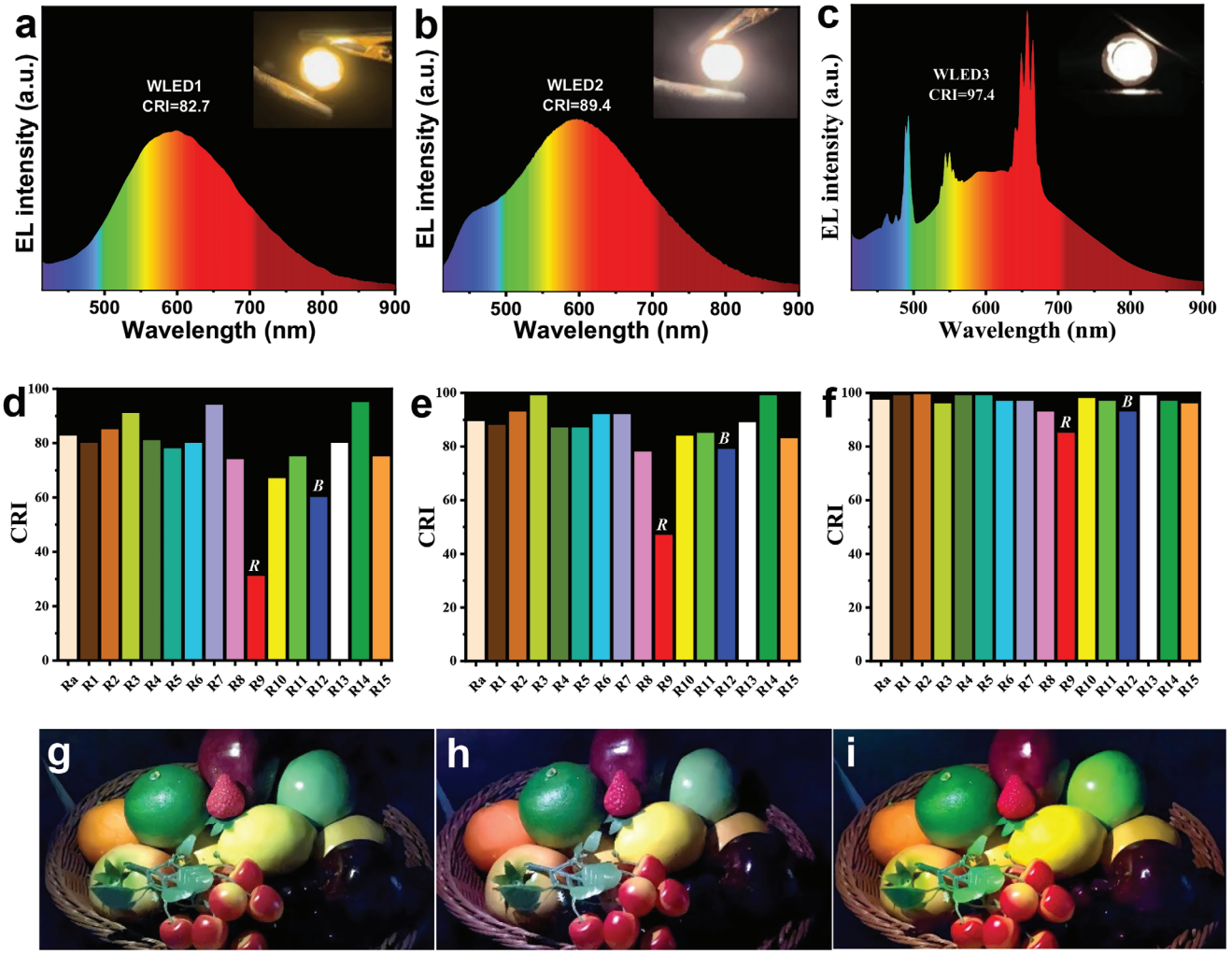

Figure 5. EL spectra of the fabricated a) WLED1, b) WLED2, and c) WLED3 using a 365 nm UV chip as the excitation source. Insets are the corresponding photographs of the working devices. d–f) R_a and R1-R15 values for the corresponding WLEDs, and g–i) the color performance of fruits under the illumination of the designed WLEDs.

(WLED2) and finally up to a record value of 97.4 (WLED3), and all the special CRI values of R1-R15 almost exceed 90 for WLED3 (Figure 5d–f). Especially, R9 and R12 representing saturated red color and saturated blue color in the WLED show significant enhancement for the Sb/Ho: $Cs_2Na_{0.9}Ag_{0.1}$(In/Bi) Cl6-based device due to the effective compensation of Sb^{3+} blue emission and Ho^{3+} red one. In addition, the associated luminous efficiency (LE) and CCT for WLED3 are 55 lm W^{-1} and 3781 K, respectively (Table S7, Supporting Information). All these parameters confirm that the fabricated WLED3 can be used for full-spectrum lighting with strict color requirements. To verify it, the pictures obtained under the illumination of three kinds of WLEDs were presented in Figure 5g–i. The images of fruits lightened by WLED3 show more realistic color as well as a more comfortable visual feeling compared to those irradiated by WLED1 and WLED2, evidencing its excellent color rendition and color saturation. Figure S16a (Supporting Information) shows EL spectra of WLED3 under different currents, and the emitting intensity gradually increases as the current rises. The stability of WLED3 is tested with the thermal imager, and it is found that the temperature is stabilized at ≈36 °C after 72 h of operation (Figure S16b, Supporting Information). The light output of WLED3 operating for 180 h has been recorded (Figure S16c, Supporting Information). Evidently, no obvious attenuation of EL intensity is detected after continuously working for 180 h for its high thermal decomposition temperature of ≈500 °C and its high thermal decomposition temperature of ≈500 °C (Figure S16d, Supporting Information). All the results confirm the stability of the investigated Sb/Ho: $Cs_2Na_{0.9}Ag_{0.1}$(In/Bi)Cl_6 phosphor and the long-term operating stability of WLED3. Therefore, it is believed that the present Sb/Ho: $Cs_2Na_{0.9}Ag_{0.1}$(In/Bi)Cl_6 DPs can be regarded as an ideal single-component white phosphor material.

3. Conclusion

In summary, we have prepared Sb/Ho: $Cs_2Na_{0.9}Ag_{0.1}$(In/Bi)Cl_6 single-component white phosphor with a high PLQY of 93% for the first time. Under UV light excitation, the product can produce

extra blue emission and red one assigned to the respective Sb^{3+}: $^3P_1 \rightarrow {}^1S_0$ transition and Ho^{3+}: $^5F_5 \rightarrow {}^5I_8$ transition in addition to the well-known broadband yellow emission of STE states. Based on experimental data and theoretical calculations, it is evidenced that the blue emission is confined within the $[SbCl_6]^{3-}$ octahedron and the red one originated from simultaneous Sb^{3+}-to-Ho^{3+} and STE-to-Ho^{3+} energy transfer. Benefited from excellent optical properties and intrinsic stability, we successfully fabricated Sb/Ho: $Cs_2Na_{0.9}Ag_{0.1}(In/Bi)Cl_6$ DP-based WLED with a record CRI of 97, CIE color coordinates of (0.39,0.38), CCT of 3781K and LE of 55 lm W^{-1}, which make it meet the requirements of high-quality commercial illumination and demonstrate its great potential in high CRI full-spectrum lighting applications.

Supporting Information

Supporting Information is available from the Wiley Online Library or from the author.

Acknowledgements

This research was supported by the National Natural Science Foundation of China (52272141, 51972060, 12074068, 52102159, and 22103012), and the Natural Science Foundation of Fujian Province (2020J02017, 2021J06021, 2021J01190, and 2020J01931).

Conflict of Interest

The authors declare no conflict of interest.

Data Availability Statement

Research data are not shared.

Keywords

double perovskites, light-emitting diodes, luminescent materials, phosphors, rare earth ions

Received: May 4, 2024
Revised: June 25, 2024
Published online:

[1] P. Pust, P. J. Schmidt, W. Schnick, *Nat. Mater.* **2015**, *14*, 454.

[2] a) S. Li, Q. Hu, J. Luo, T. Jin, J. Liu, J. Li, Z. Tan, Y. Han, Z. Zheng, T. Zhai, H. Song, L. Gao, G. Niu, J. Tang, *Adv. Opt. Mater.* **2019**, *7*, 1901098; b) Z. Xia, Q. Liu, *Prog. Mater. Sci.* **2016**, *84*, 59; c) Z. Xia, A. Meijerink, *Chem. Soc. Rev.* **2017**, *46*, 275.

[3] a) Z. Ma, Z. Shi, D. Yang, Y. Li, F. Zhang, L. Wang, X. Chen, D. Wu, Y. Tian, Y. Zhang, L. Zhang, X. Li, C. Shan, *Adv. Mater.* **2021**, *33*, 2001367; b) Y. Shao, H. Cai, F. Zhao, S. Liu, Z. Song, Q. Liu, *Inorg. Chem. Front.* **2022**, *9*, 5590; c) S. Jin, R. Li, H. Huang, N. Jiang, J. Lin, S. Wang, Y. Zheng, X. Chen, D. Chen, *Light Sci. Appl.* **2022**, *11*, 52; d) C. Dou, S. Liu, F. Zhao, Z. Song, Q. Liu, *Inorg. Chem.* **2023**, *62*, 10021.

[4] H. Zhou, P. Wu, X. Tong, H. Zhang, J. Han, X. Zhang, *Optik* **2021**, *248*, 168215.

[5] J. Zhong, J. Li, M. Liu, K. Wang, Y. Zhu, X. Li, Z. Ji, D. Chen, *J. Am. Ceram. Soc.* **2019**, *102*, 7376.

[6] A. Mao, Z. Zhao, Y. Wang, *RSC Adv.* **2017**, *7*, 42634.

[7] V. Sivakumar, U. V. Varadaraju, *J. Electrochem. Soc.* **2006**, *153*, H54.

[8] S. Yang, Z. Zhou, A. H. Li, W. Wu, *J. Lumin.* **2022**, *251*, 119104.

[9] a) S. Ye, F. Xiao, Y. X. Pan, Y. Y. Ma, Q. Y. Zhang, *Mater. Sci. Eng. R: Reports* **2010**, *71*, 1; b) F. Zhang, X. Chen, X. Qi, W. Liang, M. Wang, Z. Ma, X. Ji, D. Yang, M. Jia, D. Wu, X. J. Li, Y. Zhang, Z. Shi, C. X. Shan, *Nano Lett.* **2022**, *22*, 5046.

[10] a) X. Li, H. Liang, C. Zheng, C. Zhao, S. Bai, X. Zhao, H. Zhang, Y. Zhu, *J. Alloy. Compd.* **2023**, *966*, 171542; b) S. Jin, H. Yuan, T. Pang, M. Zhang, J. Li, Y. Zheng, T. Wu, R. Zhang, Z. Wang, D. Chen, *Adv. Mater.* **2024**, *36*, 2308487; c) S. Saikia, A. Ghosh, A. Nag, *Angew. Chem., Int. Ed.* **2023**, *62*, e202307689; d) S. Banerjee, S. Saikia, M. S. Molokeev, A. Nag, *Chem. Mater.* **2024**, 4750, https://doi.org/10.1021/acs.chemmater.4c00514.

[11] J. Luo, X. Wang, S. Li, J. Liu, Y. Guo, G. Niu, L. Yao, Y. Fu, L. Gao, Q. Dong, C. Zhao, M. Leng, F. Ma, W. Liang, L. Wang, S. Jin, J. Han, L. Zhang, J. Etheridge, J. Wang, Y. Yan, E. H. Sargent, J. Tang, *Nature* **2018**, *563*, 541.

[12] B. Zhou, Z. Liu, S. Fang, H. Zhong, B. Tian, Y. Wang, H. Li, H. Hu, Y. Shi, *ACS Energy Lett.* **2021**, *6*, 3343.

[13] X. Liu, X. Xu, B. Li, L. Yang, Q. Li, H. Jiang, D. Xu, *Small* **2020**, *16*, 2002547.

[14] X. Li, S. Xu, F. Liu, J. Qu, H. Shao, Z. Wang, Y. Cui, D. Ban, C. Wang, *ACS Appl. Mater. Interfaces* **2021**, *13*, 31031.

[15] R. Zeng, L. Zhang, Y. Xue, B. Ke, Z. Zhao, D. Huang, Q. Wei, W. Zhou, B. Zou, *J. Phys. Chem. Lett.* **2020**, *11*, 2053.

[16] J. Nie, B. Zhou, S. Fang, H. Zhong, H. Li, Y. Shi, *Chem. Mater.* **2022**, *34*, 6288.

[17] X. Li, D. Wang, Y. Zhong, F. Jiang, D. Zhao, S. Sun, P. Lu, M. Lu, Z. Wang, Z. Wu, Y. Gao, Y. Zhang, W. W. Yu, X. Bai, *Adv. Sci.* **2023**, *10*, 2207571.

[18] G. Yang, Y. Zhu, X. Li, J. Huang, X. Xu, X. Ji, A. Wang, J. Cheng, G. Pan, *Opt. Lett.* **2021**, *46*, 6043.

[19] S. Rameshkumar, *Solid State Commun.* **2023**, *376*, 115375.

[20] a) H. Tang, Y. Xu, X. Hu, Q. Hu, T. Chen, W. Jiang, L. Wang, W. Jiang, *Adv. Sci.* **2021**, *8*, 2004118; b) Y. Wu, X. Li, H. Zeng, *Small Struct* **2021**, *2*, 2000071; c) Y. Liu, X. Rong, M. Li, M. S. Molokeev, J. Zhao, Z. Xia, *Angew. Chem., Int. Ed.* **2020**, *59*, 11634; d) S. Saikia, A. Joshi, H. Arfin, S. Badola, S. Saha, A. Nag, *Angew. Chem., Int. Ed.* **2022**, *61*, e202201628; e) W. Lee, S. Hong, S. Kim, *J. Phys. Chem. C* **2019**, *123*, 2665; f) H. Arfin, J. Kaur, T. Sheikh, S. Chakraborty, A. Nag, *Angew. Chem., Int. Ed.* **2020**, *59*, 11307; g) N. Liu, W. Zheng, R. Sun, X. Li, X. Xie, L. Wang, Y. Zhang, *Adv. Funct. Mater.* **2022**, *32*, 2110663; h) Q. Chen, H. Fu, J. Jiang, Z. Fang, H. Zhang, W. Yang, W. Liu, J. Zheng, *J. Lumin.* **2023**, *258*, 119783; i) J. Sun, W. Zheng, P. Huang, M. Zhang, W. Zhang, Z. Deng, S. Yu, M. Jin, X. Chen, *Angew. Chem., Int. Ed.* **2022**, *61*, e202201993.

[21] M. B. Gray, J. D. Majher, T. A. Strom, P. M. Woodward, *Inorg. Chem.* **2019**, *58*, 13403.

[22] S. Li, Z. Shi, F. Zhang, L. Wang, Z. Ma, D. Wu, D. Yang, X. Chen, Y. Tian, Y. Zhang, C. Shan, X. Li, *ACS Appl. Mater. Interfaces* **2020**, *12*, 46330.

[23] H. Li, L. Tian, Z. Shi, Y. Li, C. Li, J. Feng, H. Zhang, *J. Mater. Chem. C.* **2022**, *10*, 10609.

[24] W. Huang, H. Peng, Q. Wei, J. Xia, X. He, B. Ke, Y. Tian, B. Zou, *Adv. Opt. Mater.* **2023**, *11*, 2203103.

[25] Z. Zeng, M. Sun, S. Zhang, H. Zhang, X. Shi, S. Ye, B. Huang, Y. Du, C. Yan, *Adv. Funct. Mater.* **2022**, *32*, 2204780.

[26] H. Xu, J. Liu, Q. Hu, J. Yu, Q. Han, W. Wu, *Adv. Opt. Mater.* **2024**, *12*, 2302288.
[27] B. Zhou, Z. Liu, S. Fang, J. Nie, H. Zhong, H. Hu, H. Li, Y. Shi, *J. Phys. Chem. Lett.* **2022**, *13*, 9140.
[28] Z. Liu, B. Zhou, S. Fang, J. Nie, H. Zhong, H. Hu, H. Li, Y. Shi, *J. Phys. Chem. Lett.* **2023**, *14*, 1022.
[29] a) S. Jin, H. Yuan, T. Pang, M. Zhang, Y. He, B. Zhuang, T. Wu, Y. Zheng, D. Chen, *Adv. Funct. Mater.* **2023**, *33*, 2304577; b) S. Jin, R. Li, J. Zhu, T. Pang, T. Wu, H. Zhan, Y. Zheng, F. Huang, X. Chen, D. Chen, *Mater. Horiz.* **2023**, *10*, 1406.
[30] M. B. Gray, S. Hariyani, T. A. Strom, J. D. Majher, J. Brgoch, P. M. Woodward, *J. Mater. Chem. C.* **2020**, *8*, 6797.
[31] J. Li, Z. Tan, M. Hu, C. Chen, J. Luo, S. Li, L. Gao, Z. Xiao, G. Niu, J. Tang, *Front. Optoelectron.* **2019**, *12*, 352.
[32] M. Jin, W. Zheng, Z. Gong, P. Huang, R. Li, J. Xu, X. Cheng, W. Zhang, X. Chen, *Nano Res.* **2022**, *15*, 6422.
[33] L. Cao, X. Jia, W. Gan, C. Ma, J. Zhang, B. Lou, J. Wang, *Adv. Funct. Mater.* **2023**, *33*, 2212135.
[34] R. D. Shannon, *Acta Crystallogr. A.* **1976**, *32*, 751.
[35] R. D. Shannon, C. T. Prewitt, *Acta Crystallogr. B.* **1969**, *25*, 925.
[36] G. Zhang, P. Dang, L. Tian, W. Yang, Z. Cheng, H. Lian, J. Lin, *Adv. Opt. Mater.* **2023**, *11*, 2202369.